Measurement of the global structure of interchange modes driven by energetic electrons trapped in a magnetic dipole

B. Levitt,[a] D. Maslovsky, and M. E. Mauel
Department of Applied Physics and Applied Mathematics, Columbia University, New York, New York 10027

(Received 14 February 2002; accepted 27 February 2002)

Measurements of the radial, azimuthal, and field-aligned mode structures of interchange instabilities excited by energetic electrons confined by a magnetic dipole are presented. The mode structures are determined using a correlation analysis of movable high-impedance floating potential probes located at various positions within the plasma. The hot electron population, produced by electron cyclotron resonance heating, becomes unstable to hot electron interchange (HEI) instabilities which saturate nonlinearly with a complex and time-varying frequency spectrum. Although the mode frequencies vary dramatically, it is found that the mode structures do not evolve significantly in time, being determined by the azimuthal mode numbers. These measurements are compared to a self-consistent nonlinear particle simulation of the HEI mode in dipole geometry. Upon appropriate adjustment of the boundary conditions, the simulation reproduces the measured radial and azimuthal structures at large amplitudes. © *2002 American Institute of Physics.* [DOI: 10.1063/1.1475999]

I. INTRODUCTION

Interchange, or ''fluting,'' instabilities in magnetized plasma are among the best known in plasma physics.[1–4] Interchange motion mixes plasma contained by magnetic flux tubes while minimizing changes in the magnetic field. Instability results when the mixing reduces the plasma's potential or kinetic energy. This occurs for various reasons in the laboratory, the ionosphere, and in planetary magntospheres. In laboratory plasmas, interchange instabilities are possible when the pressure gradient has components parallel to the magnetic curvature. Experiments have shown them to be stabilized by reversing the direction of curvature,[5,6] by creating ''average good curvature'' either on toroidal flux surfaces[7] or on the plasma-vacuum boundary,[8] and by creating local regions with average magnetic shear.[9] In the ionosphere, gravity drives interchange instability, and its nonlinear evolution plays an essential role in the intense wave dynamics of the night-time equatorial F region.[10] Interchange motion of plasma confined by the dipole-like field of planetary magnetospheres can be driven or ''spontaneous'' (i.e., unstable), and both have been extensively studied theoretically.[11–13] Because the magnetic field strength of a dipole decreases rapidly with radius, $B \sim R^{-3}$, interchange motion in a dipole is associated with significant plasma compression. Pressure gradients can drive interchange instability in a dipole only when the equatorial plasma pressure profile varies more rapidly than $p \sim R^{-4\gamma}$ (where $\gamma \approx 5/3$ is the appropriate MHD ratio of specific heat). Observations show the Earth's magnetosphere to be interchange stable, but steady plasma circulation and impulsive radial-diffusion[14] results from electric fields created by the solar wind, and these can be considered examples of driven interchange motion. In Jupiter's magnetosphere, interchange instability is influenced by pressure gradients and by centrifugal forces caused by co-rotation.[15] Recently, the Galileo spacecraft measured a buoyant, inward-moving flux tube within Jupiter's Io plasma torus and also fluctuations in the bulk ion flow and density that provide evidence for unstable interchange motion of dipole-confined plasma in space.[16–18]

Although interchange instability is an important process for magnetized plasma, measurement of its global structure has been possible in only a few cases. Probably, the most detailed images of interchange instability have been made from radio-wave scattering from the F layer and the ionosphere. (See Kelly's monograph.[10]) These spectacular images show towering ''plumes'' created by rising interchange ''bubbles.'' Nonlinear simulation of the gravitational interchange has reproduced this plume structure.[19] Laboratory observations of the nonlinear structures of interchange instability have also been made using toroidal devices that have regions without magnetic shear. The electrostatic potential has been mapped using movable floating potential probes in a toroidal octopole[9,20] and in current-free discharges created in a purely toroidal magnetic field.[21,22] These electrostatic potential structures sometimes form closed equipotential contours that appear as slowly propagating and coherent $\mathbf{E}\times\mathbf{B}$ vortices, or ''convective cells.'' They decay by viscous forces if not continuously driven. For plasma formed within a purely toroidal magnetic field, the electrostatic potential evolves into a highly nonlinear state dominated by a rotating dipole vortex superimposed on equilibrium poloidal flows that have been reproduced by self-consistent, nonlinear simulation.[23]

When interchange instabilities are excited by magnetically trapped energetic electrons, the modes have a real frequency proportional to the fast ∇B drift of the hot electrons, ω_d. When the rotation frequency is less than the ion-cyclotron frequency, the instability is called the low-frequency hot electron interchange (HEI) instability.[24]

[a]Electronic mail: bl187@columbia.edu

Higher frequency modes have been described by Berk,[25] and both the low-frequency and high-frequency hot electron interchange mode have been identified experimentally.[26–28] Hot electron plasmas can remain stable even when pressure gradients exceed the usual MHD condition of flute instability because the real frequency of the mode generates stabilizing ion polarization currents. Although the global mode structure was not measured directly in these previous studies, Spong and co-workers[29] showed that when realistic profiles are used during computation of the linear, radial eigenmode, then the predicted onset for instability was consistent with experimental observations.

In this paper, we present the first measurements of the mode structure of the electrostatic, low-frequency interchange instability driven by energetic electrons trapped in an axisymmetric dipole magnetic field. The modes rotate rapidly in the drift direction of the trapped electrons, and they have a complex and time-varying frequency spectrum. Several modes co-exist. Experimentally, these modes are distinguished from each other using frequency-domain correlation between several movable probes and a fixed reference probe. The measurements show the flute-modes have a radial structure that depends only on the azimuthal mode number, m, extends across the entire dipole-confined plasma, and does not evolve in time with the frequency. In this paper, we also compare these measurements to a fully self-consistent, nonlinear simulation that has been described elsewhere.[30] The simulation reproduces both the large-amplitude mode structure of the interchange modes and their complex, time-varying frequency spectra.

In previous papers, we described the collisionless particle transport induced by the hot electron interchange instability.[31–33] For charged particles deeply trapped by a strong dipole magnetic field, the frequencies of the three characteristic periodic motions, cyclotrons, ω_c, bounce, ω_b, and magnetic drift, ω_d, are well-separated, and the corresponding actions, the magnetic moment, μ, the longitudinal adiabatic invariant, J, and the magnetic flux, ψ, are approximately constant. Low-frequency interchange fluctuations break the third adiabatic invariant, ψ, through resonant interaction, $\omega \sim m\omega_d$, with the rotating potential structures. Rapid global transport only occurs when the interchange mode spectrum causes resonance overlap,[35] and this has been demonstrated in the laboratory.[31–33] Since $\omega \ll \omega_b \ll \omega_c$, μ and J remain constant even when the radial transport is chaotic.[34] In our simulations, invariance of (μ, J) serves as the ''equation of state'' for modeling adiabatic, collisionless heating or cooling during the radial flute motion of the energetic electrons induced by electrostatic fluctuations in a dipole.

The agreement between the measured mode structure and the predictions from the self-consistent description of the growth of the interchange instability also adds support for a nonlinear explanation for the observed rising frequency, or ''chirps,'' of the electrostatic interchange instability in a dipole. Berk and co-workers[36,37] showed that nonlinear phase-space structures (called ''clumps'' and ''holes'') will form spontaneously for a resonant wave-particle instability held near marginal stability by nonresonant dissipation. At large amplitudes, nonlinear interactions overwhelm the dissipation causing frequency sweeping and new modes to be excited. The strong resonant interactions between collisionless dipole-confined energetic electrons and rotating interchange modes are particularly easy to apply the formulation used by Berk.[30] This is because the wave-particle dynamics is one-dimensional, and the two-dimensional phase-space is directly observable. (The guiding-center Hamiltonian phase-space coordinates for drift motion in an axisymmetric dipole are the angle of symmetry, φ, and the magnetic flux, $\psi \propto 1/R$.) Berk's explanation for the rising frequency of the interchange instability seen in the experiment corresponds to the inward propagation of ''holes'' in the phase-space of the energetic electrons. These holes are seen in the simulation and appear in the laboratory as deep modulations of energetic electron current collected with gridded probes.[30] It is interesting that these resonant phase-space holes are much more dynamic and radially complex than the global potential structure of the interchange instability that creates them. When the electrostatic interchange mode is driven by energetic electrons, it is the electron's resonant phase-space that contains strong $\mathbf{E}\times\mathbf{B}$ vortices[38]—not the mass flow. Since there is a distribution of electron energy and, consequently, of electron drift velocity, ω_d, the location and size of holes (or vortices) are energy dependent. Furthermore, the energetic electrons cause the instability to rotate quickly in the ion's frame of reference. The plasma mass density does not circulate fully around the equipotential contours (as seen, for example, in the laboratory experiment with a purely toroidal field). Instead, the ion density is radially ''stirred'' as the interchange mode structure rotates by.

The outline of this paper is as follows. Section II describes the Collisionless Terrella Experiment (CTX) used to observe the hot electron interchange instability. Here, we also describe the floating potential probe measurements and the frequency-domain correlation method used to reconstruct the radial, azimuthal, and field-aligned mode structure. Section III summarizes the observations of the hot electron interchange mode at large amplitude. The lowest azimuthal modes are most readily detected, and rotating modes with $m=1$, 2, and 3 are described. In each case, the mode is flute-like and rotates rigidly. Section IV describes the self-consistent nonlinear simulation used to interpret the measurements. Both the model equations and the numerical method are briefly described. The simulation reproduces measurements of the radial mode structure, overall amplitude, and the observed frequency sweeping. Finally, we summarize our results and describe some on-going efforts that will further investigate interchange motion in dipole magnetic fields.

II. EXPERIMENTAL METHODS

The measurements reported here were made using the Collisionless Terrella Experiment, CTX.[32] The CTX device consists of an ultrahigh vacuum chamber, 140 cm in diameter, and a mechanically supported dipole electromagnet. A stainless steel enclosure electrically grounded to the chamber

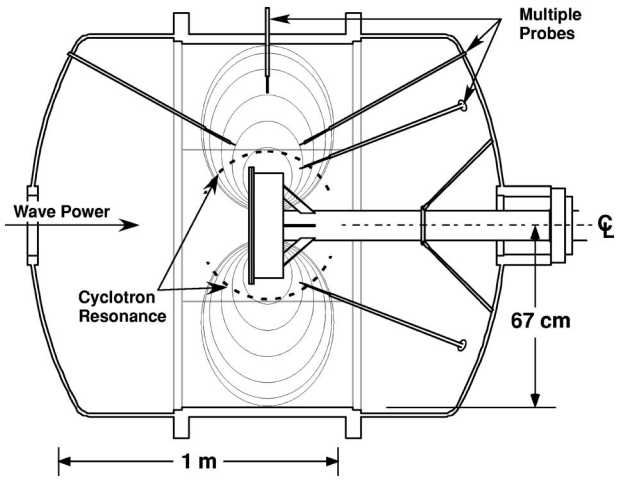

FIG. 1. Schematic of the CTX vacuum chamber, depicting the five moving floating potential probes used to measure the electrostatic fluctuations.

TABLE I. Key parameters used to define the dimensions of the electrostatic dipole simulation.

Dimension	Meaning	Typical value
L_0	Hot electron location	27 cm
B_0	Equatorial field strength	875 G
ψ_0	Magnetic flux, $B_0 L_0^2$	6×10^5 Maxwells
M_0	Characteristic dipole magnetic moment, $B_0 L_0^3$	1.7×10^7 G cm^3
μ_0	Characteristic hot electron magnetic moment	9×10^{-12} erg/G
$\mu_0 B_0$	Hot electron energy	8×10^{-9} erg (5 keV)
ω_{dh0}	Precession frequency, $(3c/e)\mu_0 B_0/\psi_0$	$2\pi\times0.4$ Mrad/s
ω_{dh0}^{-1}	Time (angular)	0.4 μs/rad
n_0	Plasma density	1.0×10^{10} cm^{-3}
N_0	Particle number per unit flux, $n_0\delta V_0 = 0.91 n_0 L_0/B_0$	2.8×10^8 Maxwell^{-1}
L_0^2/λ_{D0}^2	Normalized Debye length	2.6×10^3
$\omega_{ci0}/\omega_{dh0}$	Normalized ion cyclotron frequency	3.5

wall surrounds the magnet, which has a maximum magnetic field strength at the face of the terrella of 15 kG and decreases to 50 G at the vessel wall.

The electrostatic fluctuations are measured by five high impedance floating potential probes located at various positions in the vacuum chamber. Each probe tip consists of a 1 mm stainless steel wire connected to a 100 kΩ resistor and 50 Ω coaxial cable contained within a ceramic tube. The fluctuating signals from the probe are amplified with impedance-matched wide-bandwidth amplifiers and digitized with high-speed, 8-bit digitizers. These probes can be repositioned radially to examine either potential fluctuations at different positions on the same field line or fluctuations on different field lines separated radially or separated azimuthally by 90° or 180°. A schematic of the experiment showing a representative probe arrangement is shown in Fig. 1.

Hot electron plasma is created by applying a microwave heating pulse lasting from 0.5 to several seconds. The power source is a continuous wave magnetron with a power output of 1.0 kW at a frequency of 2.45 GHz. The microwave pulse ionizes hydrogen from a short gas puff and heats magnetically trapped electrons at the cyclotron resonance. The fundamental microwave cyclotron resonance is a surface, approximately spherical, that is defined by $B_0 \equiv 875$ G and that intersects all of the field-lines of the dipole that cross the equator with radius, $R \geqslant R_0 \equiv 27$ cm. Electrons trapped on any of these field lines can absorb power from the microwaves, but those electrons located on field lines with an equatorial radius $R \approx R_0$ have a resonance at the field minimum and are heated most strongly. A fraction of these become deeply trapped and energetic (and with anisotropic velocity, $\mu B \gg \omega_b J$), and we refer to these electrons as an ''artificial radiation belt.'' Bremsstrahlung radiation characterizes the energetic electrons. As seen in other hot-electron microwave discharges,[26] the energetic electrons have a nonthermal, power-law, energy distribution with energies from a few keV and extending to more than 40 keV.[32] The intensity of the energetic electron population depends on the strength of the hydrogen gas puff. We find the energetic electron density and energy is maximized with a hydrogen pressure of $\sim 1\times10^{-6}$ Torr, and this is the value used for the experiments reported here. When the microwave power is switched off, the trapped electrons persist while the density of colder electrons decays. This creates a so-called ''afterglow'' that lasts for several tens of milliseconds.

Parameters characterizing the plasma studied here are summarized in Table I. An energy of 5 keV is used to characterize the energetic electron distribution even though these electrons have a non-Maxwellian distribution. The plasma and energetic electron densities are maximum at 27 cm, and the plasma density is estimated to be roughly 10% to 20% of the cutoff density, or approximately 1×10^{10} cm^{-3}. Within the plasma, the neutral density is significantly reduced from the value outside the plasma; nevertheless, for these low-density plasmas, collisions with neutrals dominate over charged-particle collisions for the energetic electrons. For 5 keV trapped electrons, the magnetic drift frequency is $\omega_d/2\pi = 3.7\times10^5$ s^{-1}, and we estimate $\omega_d \tau_{\rm col} \geqslant 100$. Also, for these particles, the normalized gyroradius is $\rho/R_0 \sim 0.01$; therefore, the trapped electrons are adiabatic and exhibit well-separated cyclotron, bounce and drift frequencies, $\omega_d/\omega_b \sim \rho/R_0$.

A. Observation of HEI instability

In the presence of an intense hot electron population, drift-resonant ($\omega \sim \omega_d$) fluctuations are observed, both during and after the microwave heating pulse. Some characteristics of the fluctuations in these two time periods are different. With the heating on, the fluctuations appear as repetitive short bursts, 300–500 μs, while during the afterglow they may last as long as several ms. In addition, the afterglow fluctuations have a higher frequency, with coherent modes rising in time up to 20 MHz. During the heating regime, the fluctuations are generally observed to have $f \leqslant 5$ MHz and have a more dynamic, rapidly changing spectral content. In both intervals, the frequency spectrum is complex and time-varying, exhibiting rising tones in time.

Figure 2 shows the floating potential fluctuations on various relative time scales. The first figure shows a long

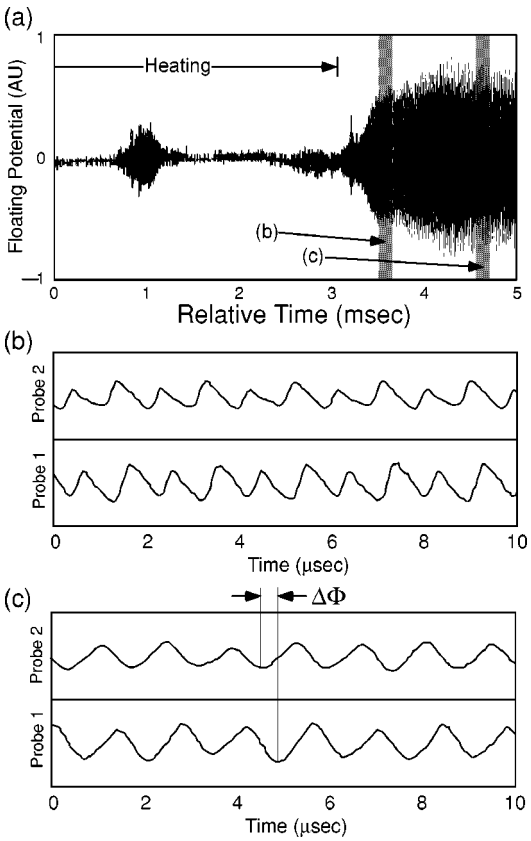

FIG. 2. Floating potential probe signals of the drift-resonant instability on different time scales. (a) A long time scale shows an instability burst during heating and a saturated mode during the afterglow. On a faster time scale, (b) and (c), show the nonsinusoidal wave forms from two spatially separated high-impedance probes that illustrate the phase difference between probes.

time scale, and instabilities are present both during heating and during the afterglow. The mode amplitude typically saturates at a level between 100–200 V. On a faster time scale, the fluctuations are seen to be nonsinusoidal and slowly change in time. This change represents the presence of multiple azimuthal modes with frequencies that evolve at different rates. When the same fluctuations are observed by two probes that are azimuthally separated by 90°, the phase difference indicates a low-order mode structure that rotates in the direction of the electron ∇B drift.

B. Correlation analysis

Five movable high impedance floating potential probes (with 100 kΩ tips) are located at various positions in the plasma. These probes are used to reconstruct the mode structure using cross-correlation analysis of combinations of probe pairs and a fixed ''reference'' probe. Although the movable probes can access regions extending from the dipole magnet to the vacuum chamber wall, measurements are possible only when the probe's location does not interfere with the bulk of the energetic trapped electrons. Referring again to Fig. 1, four of the five probes are inserted at a $\pm 30°$ angle with respect to the dipole's axis. These probes can be inserted very near the electron cyclotron resonance ($R \sim 27$ cm) since the most deeply trapped electrons have insufficient parallel velocity to strike the probe. In contrast, the probe inserted at the equator can be inserted only to approximately $R \geqslant 45$ cm.

Since the magnetic field line geometry is known, the probe positions can be expressed with a geometric labeling of the magnetic coordinates in analogy with McIlwian.[39] The radial coordinate for a field line is its equatorial distance, R. Distance along a field line is labeled by s, and the azimuthal coordinate is φ. The measured probe position is mapped to its equivalent magnetic coordinate, (R,φ,s), by numerical computation. Because the plasma pressure is low and because most of the plasma volume is sufficiently far from the dipole electromagnet, the field lines follow approximately the trajectories from a point dipole in vacuum. The CTX dipole moment is $M_0 = B_0 R_0^3 = 1.7 \times 10^7$ G cm^3, and an approximate relation exists between (R,φ,s) and the usual magnetic coordinates for a point dipole, (ψ,φ,χ), defined by $\mathbf{B} = \nabla\varphi \times \nabla\psi = \nabla\chi$, where χ is the magnetic scalar potential. This relationship is simply $(R,\varphi,s) \approx (M_0/\psi, \varphi, \int d\chi/B)$.

Measurement of the mode structure is complicated by the simultaneous presence of several modes, but it is simplified because the phase of the potential is constant along the field line. The quantities to be measured are expressed in terms of a modal prescription for the voltage measured by a probe located at (R,φ,s),

$$\Phi(R,\varphi,s,t) \equiv \sum_{n,m} \Re\{\Phi_{n,m}(R,t) \times \exp[i(m\varphi + k_\parallel s + k_R R - \omega_n t)]\}, \qquad (1)$$

where n is the mode index, and $k_\parallel$, k_R, and ω_n may be slow functions of time. The amplitude, $\Phi_{n,m}$ changes slowly in time, but we find it does not change in spatial structure. We also find the $|\Phi|$ does not change significantly with s over the region accessible with the probes. These observations justify the modal prescription *a posteriori.*

When the digitized signals from two probes are Fourier transformed, the transform of the correlation between two probes, $C(1,2)$, is expressed as the product of one probe signal with the complex conjugate of the second. In terms of the modal prescription, this correlation is

$$C_{n,m}(1,2) \approx \Phi_{n,m}(R_1)\Phi^*_{n,m}(R_2) \times \exp[i(m\Delta\varphi + k_\parallel \Delta s + k_R \Delta R)]. \qquad (2)$$

Since $\Delta s = s_1 - s_2$ and $\Delta R = R_1 - R_2$ are known, the phase of the correlation can be used to determine, m, $k_\parallel$, and k_R. Our ability to use Eq. (2) for mode analysis improves as the time rate of change of the mode frequency vanishes, $\partial\omega/\partial t \equiv \dot{\omega}_n \to 0$, or as the frequency separation between nearby modes becomes large. This is because we must Fourier transform the digitized wave forms with finite time windows. Because the mode frequency is not constant, a simple fast Fourier transform cannot be used to transform the probe signals. Instead, the slow-time evolution of the mode spectrum is computed using short-time Fourier transforms with a continuously moving triangular (or ''Parzen'') window, referred to as a spectrogram or a time-frequency-domain (TFD) signal representation.[32] The TFD of $C(1,2)$ is computed from

the product of the short-time fast-Fourier transforms of two probes using identical, moving time windows. Because the mode frequency evolves more quickly during microwave heating than during the afterglow, the time windows can be longer and the mode frequencies better identified during the afterglow.

III. MEASUREMENT OF GLOBAL MODE STRUCTURES

The overall procedure for measurement of the global mode structure can now be described. First, three probes are placed at the same azimuth, φ, and adjusted radially to be located on the same field line, R. The relative amplitude of the Fourier transform of the correlation of any two of these probes is used to determine the variation of $|\Phi_{n,m}|$ along the field, and the variation of the phase is used to measure $k_{\|}\Delta s$. This measurement was important since it established the flute-like nature of the electrostatic fluctuations and simplified the analysis of the following measurements. We find $k_{\|} \approx 0$ for all modes, and the amplitude varies by less than 10% between the three probes. The second part of the procedure uses three probes to determine k_R and m from the phases of the correlations of two separated probes with a fixed reference probe located at $R=49$ cm. Since these probes are located at different R, the phase information is meaningful only if the magnitudes of the correlations between all probes is large. Since the mode structures are broad, we find significant correlation for all modes and for all probe separations. The final step determines the radial variation of the mode amplitude by correlation analysis of a probe that is moved in increments approximately $\delta R \sim 2$ cm for successive plasma discharges. The ratio of (1) the correlation between this moving probe and the fixed reference probe and (2) the self-correlation of the reference probe results in the normalized radial mode structure for any given mode. This is defined as $\Phi_{nm,}(R_2)/\Phi_{n,m}(R_1) \equiv |C(1,2)|/|C(1,1)|$, and the profile is obtained as the position of the second probe, R_2, is moved relative to the fixed position of the first probe, R_1.

In order to illustrate the complexity of the frequency spectrum, the time-frequency domain of the magnitude of the correlation between two probes separated only in azimuthal angle is shown in Fig. 3. In this example, $\Delta R \sim \Delta s \sim 0$, and $\Delta\varphi = 90°$. The figure shows the slow evolution of the potential oscillations during the afterglow, $\dot{\omega}_n/\omega_n^2 \sim 2\times 10^{-4}$. The modes with larger amplitudes are labeled by their azimuthal mode numbers, m. Note several modes exist simultaneously with the same azimuthal mode number but with different frequencies. For example, three modes with $m=1$, $m=2$, and $m=3$ are identified. The frequencies of harmonic modes evolve in time at rates different from the fundamental, and this corresponds to the time evolution of the nonsinusoidal wave form of the potential. An example of this harmonic structure are the modes at approximately 2.4, 4.7, 7.0, and 9.4 MHz. Many modes with different m do not appear to be harmonically related (i.e., the ratio of frequencies are not rational numbers). For example, several $m=1$ modes coexist near 1 MHz. The low frequency, $m=1$, modes usually have the largest magnitude, but this is not always the case. The amplitudes of harmonic modes usually decrease with increasing frequency.

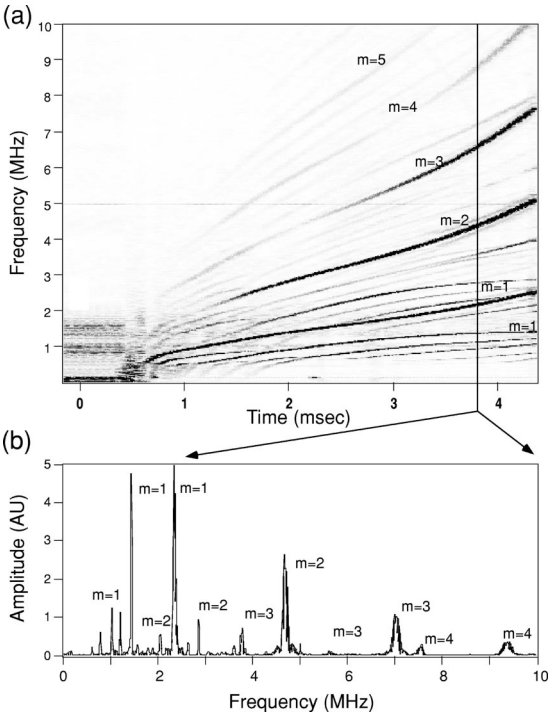

FIG. 3. TFD of the magnitude of the correlation function of two floating potential probes with $\Delta R = \Delta s = 0$ and $\Delta\varphi = 90°$ graphed with a linear gray scale. Shown below is the short-time frequency spectrum of the correlation at an instant during fully developed and saturated oscillations. The azimuthal mode numbers are shown.

The relative amplitudes of the modes change appreciably in time, as can be seen from the TFD of the correlation magnitude. Often, the higher m modes begin to increase in magnitude as the mode evolves while the amplitude of the prominent $m=1$ mode gradually decays. Sometimes the $m=1$ and $m=2$ modes have equal amplitude, and occasionally, the $m=2$ dominates. This observation necessitates our measurement of the normalized structure for each azimuthal mode using correlation analysis with the fixed reference probe. The radial mode structure must be reconstructed from many similarly prepared discharges, but the relative amplitudes of the modes as well as their frequencies at any instant are never the same from discharge to discharge. However, we find the amplitude for any given mode at any given position relative to the amplitude of the fixed reference probe to be essentially time invariant.

While two probes azimuthally separated were used to determine m, other probes positioned on the same field line were used to determine the field-aligned mode variation. For example, Fig. 4 illustrates the phase difference between two probes with $\Delta R = \Delta\varphi = 0$, $R=49$ cm, and $\Delta s = 35$ cm. These measurements were made for the same discharge as illustrated in Fig. 3, and Fig. 4 shows the phase difference, $k_{\|}\Delta s$, for the largest amplitude, $m=1$ mode as a function of time. Similar analyses were made for other modes, and all modes show a constant phase structure along a field line. Since the equatorial probe was used for these measurements, only field lines having $R > 45$ cm could be accessed without perturbing

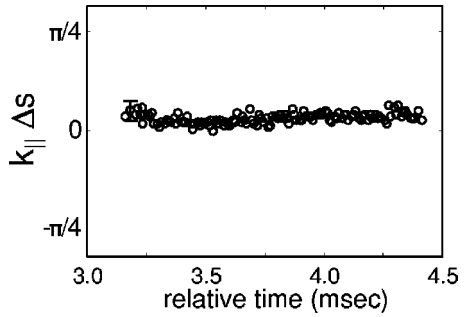

FIG. 4. The field-line phase difference of the correlation function for two probes positioned at two locations along the same field line, $\Delta R=\Delta\varphi=0$ and $\Delta s\approx 35$ cm, showing $k_{\|}\approx 0$ for several modes during the afterglow.

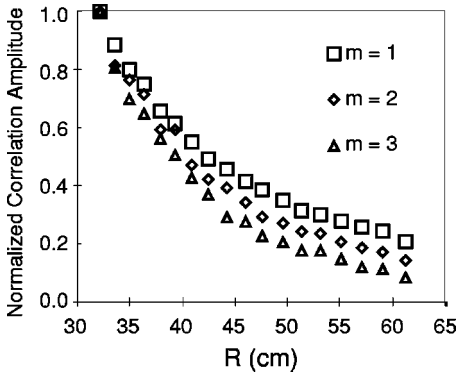

FIG. 6. Radial profiles of normalized correlation amplitudes, $|C_{n,m}(1,2)|/|C_{n,m}(1,1)|$, for the lowest three azimuthal modes.

the energetic trapped particles. The probe positions were approximately $s\sim 0$ and $s=\pm 35$ cm, and, for these positions, we find the relative mode amplitudes are comparable to within $\pm 10\%$. These measurements indicate the potential fluctuations are flute-like.

The final step in mode measurement procedure is to analyze the relative phase and amplitude of the correlation of two probes with increasing radial separation. Probes located off the equatorial midplane were used (see Fig. 1) since these probes could be inserted deep into the plasma and near to the dipole magnet without disturbing the energetic electrons or the potential fluctuations observed by the reference probe. By using multiple probes, correlation analysis of the TFD identified both the azimuthal mode and the radial variations. Since $k_{\|}\sim 0$ and since m is known, probes located at any position within the plasma can be used to compute the radial correlations.

Figures 5 and 6 show the results of these measurements. In Fig. 5, the three lowest m numbers were examined at three different times in a single discharge but with each radial location representing averages of several shots having the movable probe at different positions. We observe no apparent time dependence in the phase, and there is no change in the phase with radius. Since $k_R\sim 0$, the mode structures rotate rigidly. In Fig. 6, the radial profile of the normalized magnitude of the two-probe correlation shows the radial structure to be broad and to depend weakly on the azimuthal mode. Higher m modes are seen to be more localized toward the core, as might be expected. In all cases, the mode structure extends from the edge to the inner hot electron region, and they are not localized to particular flux surfaces. In addition, no time dependence is observed in these normalized profiles, although the relative amplitudes of one mode with the other are observed to vary in time. In making these observations, we find it noteworthy that the global mode structures are time-independent despite the complex and time variation of the fluctuation's frequency spectrum.

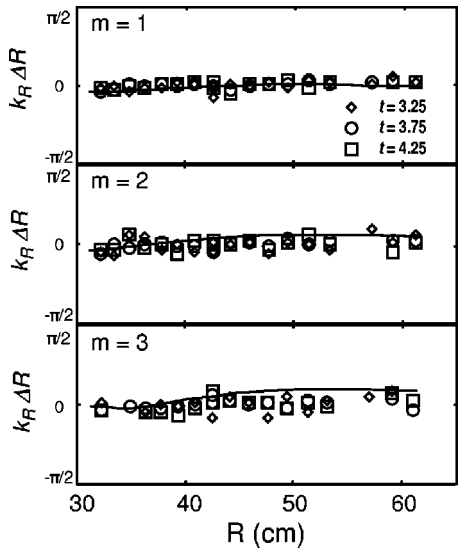

FIG. 5. The phase of the correlation between two probes as the radial separation increased for the lowest three azimuthal modes. Results show $k_R\approx 0$ for all modes during the afterglow. Solid lines are the relative phase difference of global modes computed from the nonlinear simulated (Sec. IV C).

Finally, equivalent measurements were made of the global mode structure of the bursting interchange instabilities observed during microwave heating. As described by Warren,[32] clearly identified modes with well-separated frequencies are observed during the second half of every burst. The rate of change of the mode frequencies are approximately $\dot{\omega}_n/\omega_n^2\sim 0.2$, considerably faster than during the afterglow. Nevertheless, modes with $m=1$ and $m=2$ were identified. We found the radial structure for these modes to be the same as shown in Fig. 6; however, averaging over discharges showed a larger variance especially for the radial variation of the phase, $k_R\Delta R$.

IV. MODELING THE NONLINEAR EVOLUTION OF THE HEI INSTABILITY

This section describes the nonlinear, self-consistent simulation of the time evolution of the hot electron interchange (HEI) instability used to interpret measurements of the global mode structure. Previously, Ref. 30 described this simulation together with the linear dispersion relation for HEI instability in a dipole-confined plasma. For completeness, we review again the basic model equations and, then, describe more fully the numerical procedure used to compare simulation with measurement.

The simulation solves finite-difference approximations to the coupled, nonlinear model equations for the evolution

of the electrostatic potential and the field-line integrated number densities of ions and energetic electrons. The simulation is similar to those described by Refs. 19 and 23. The electrostatic potential is advanced by solving the equation for charge continuity subject to reasonable boundary conditions. However, unlike these other nonlinear simulations, multiple groups of particles must be evolved simultaneously in order to capture the drift resonance between the energetic electrons and the azimuthal propagation of the interchange instability. References 19 and 23 required only a single equation for the mass density; whereas, simulation of the HEI instability additionally requires evolving the phase-space density of several groups of energetic electrons, each having different values of the magnetic moment, μ. Finite-difference approximations to the model equations are integrated using the numerical methods introduced by Zalesak[40,41] and following an implementation demonstrated by Guzdar and co-authors.[42]

A. Model equations

The model equations are described in the coordinates of an ideal, axisymmetric dipole magnetic field. The potential, $\Phi(\psi,\varphi,t)$, is assumed constant along a field line, consistent with measurements and our understanding of interchange instability. The potential evolves in time due to the divergence of net perpendicular current integrated over magnetic flux tubes and subject to fixed boundary conditions. The divergence of perpendicular current either charges or discharges flux tubes. Energetic electrons contribute to this current through the ∇B drift, and ions contribute through the polarization or inertial drift. In order to simplify the computation of energetic electron dynamics, the energetic electrons are assumed to be deeply trapped with negligible motion along field lines, $J\sim 0$. A neutralizing population of cold electrons exists that is more uniformly distributed along the field line. Finally, to facilitate an efficient spectral solution for the potential, we define an axisymmetric dielectric, $\bar{\varepsilon}(\psi,t)$, proportional to the azimuthally averaged ion number per flux tube, $\bar{N}_i(\psi,t)=\int d\varphi\, N_i/2\pi$.

Using the notation in Ref. 30, the flux-tube average is defined as $\langle A\rangle \equiv \delta V^{-1}\int d\chi\, A/B^2$, where $\delta V(\psi)=\int d\chi/B^2$ is the volume of a flux tube of given flux, $d\psi\, d\varphi$. The model equations describe only the dynamics of the total particles on a tube of unit flux, $N\equiv\langle n\rangle \delta V$, but the particle density n, can vary along a field line. Since the magnetic field of the point dipole is relatively simple to characterize, expressions for the field-line integrals can be computed after making reasonable assumptions for the field-line density profile.

Effectively, there are three coupled, nonlinear equations to be solved in the simulation. These are the time evolution of the potential, $\delta V\langle\nabla\cdot\nabla\dot{\Phi}\rangle=-4\pi e(\dot{N}_i-\dot{N}_e)\equiv -4\pi e\Delta\rho$, the evolution of the ion number, $\dot{N}_i=-\delta V\langle\nabla\cdot n_i\mathbf{V}_i\rangle$, and the evolution of several populations of energetic electrons having different magnetic moments, $\langle\dot{n}_e\rangle\delta V\equiv\dot{N}_e=\Sigma_\mu F_\mu(\psi,\varphi,t)$. To denote the time derivative, we use $\dot{A}\equiv\partial A/\partial t$. The rate of change of net charge on a flux tube due to the integrated divergence of the perpendicular current is $\Delta\rho$. In the expression for the electrons, F_μ is the number of electrons with a given μ on the given flux tube. $F_\mu(\psi,\varphi,t)$ is a bounce-averaged phase-space density that evolves according to the guiding center drift Hamiltonian.[32]

The field-line integral of the ion current depends upon the density profile along the field line. We call this integral the density-weighted average, defined as $\|A\|\equiv\langle An\rangle/\langle n\rangle = N^{-1}\int d\chi\, n(\chi)A/B^2$. In this notation, the ion continuity equation is

$$\frac{\partial N_i}{\partial t}+\frac{\partial}{\partial\varphi}(N_i\|\nabla\varphi\cdot\mathbf{V}_i\|)+\frac{\partial}{\partial\psi}(N_i\|\nabla\psi\cdot\mathbf{V}_i\|)=0. \tag{3}$$

For cold ions and for low-frequency interchanges with $\omega\ll\omega_{ci}$, $\mathbf{V}_i$ is the sum of the $\mathbf{E}\times\mathbf{B}$ and polarization drifts. This substitution gives

$$\frac{\partial N_i}{\partial t}+\frac{\partial}{\partial\varphi}\left[cN_i\left(-\frac{\partial\Phi}{\partial\psi}-\left\|\frac{|\nabla\varphi|^2}{\omega_{ci}B}\right\|\frac{\partial\dot{\Phi}}{\partial\varphi}\right)\right] + \frac{\partial}{\partial\psi}\left[cN_i\left(\frac{\partial\Phi}{\partial\varphi}-\left\|\frac{|\nabla\psi|^2}{\omega_{ci}B}\right\|\frac{\partial\dot{\Phi}}{\partial\psi}\right)\right]=0. \tag{4}$$

The first term in parentheses is the $\mathbf{E}\times\mathbf{B}$ drift, and the second term is the polarization drift. This second term represents the plasma dielectric response, and the azimuthal average of this term will serve as the dielectric, $\bar{\varepsilon}$, when solving for $\dot{\Phi}$.

Since the field-line profile of the plasma density is not known, we invoke an important simplification in order to compute the density-weighted integrals. The density profile is assumed to be relatively broad and vary on all field lines as $n\propto\sin\theta$, where θ is the polar angle from the dipole's axis. For a point dipole, the magnetic coordinate, χ, is related to the polar angle as $\chi=(\psi^2/M_0)\cos\theta/\sin^4\theta$. With this density profile, the density-weighted averages are $\||\nabla\varphi|^2/\omega_{ci}B\|\approx 0.66M_0^2B_0/\psi^4\omega_{ci0}$ and $\||\nabla\psi|^2/\omega_{ci}B\|\approx 0.77M_0^2B_0/\psi^2\omega_{ci0}$, where ω_{ci0} is the ion cyclotron frequency at $B=B_0$.

The field-line integrals of the Laplacian in the equation for the potential take a particularly simple form in dipole magnetic coordinates. The linear Poisson's equation becomes

$$h_\varphi\frac{\partial^2\Phi}{\partial\varphi^2}+h_\psi\frac{\partial^2\Phi}{\partial\psi^2}=-4\pi e(N_i-N_e)\equiv -4\pi e\rho, \tag{5}$$

where $\rho(\psi,\varphi,t)$ is the net charge on a field line. Two geometric terms define the transformation of the Laplacian operator into field-line averaged flux coordinates: $h_\varphi\equiv\int d\chi/|\nabla\psi|^2=2M_0/\psi^2$ and $h_\psi\equiv\int d\chi/|\nabla\varphi|^2=4M_0$.

The electrons are grouped by magnetic moment, or effective energy μB_0, and separate evolution equations are needed for each energetic electron group. The collisionless guiding-center evolution of electrons with constant moment μ is governed by the following equation:

$$\frac{\partial F_\mu}{\partial t}+\frac{\partial}{\partial\varphi}\left[\left(\omega_d(\mu,\psi)-c\frac{\partial\Phi}{\partial\psi}\right)F_\mu\right]+\frac{\partial}{\partial\psi}\left[c\frac{\partial\Phi}{\partial\varphi}F_\mu\right]=0. \tag{6}$$

Equations (4) and (6) and the time derivative of Eq. (5) can be combined to form the equation used to evolve the electrostatic potential. This requires proper treatment of the

ion polarization currents. For our simulation, we desire to preserve the form of the Laplacian operator since this form can be inverted easily. We achieve this by defining an ''axisymmetric'' dielectric constant, $\overline{\varepsilon}$, in terms of the azimuthal average of the ion number, $\overline{N_i}$. The remaining nonaxisymmetric part is defined as $\tilde{N}_i \equiv N_i - \overline{N_i}$. Using these definitions, the equation for the evolution of the potential used in the numerical simulation is

$$h_\varphi \overline{\varepsilon}_\varphi(\psi,t)\frac{\partial^2 \dot{\Phi}}{\partial \varphi^2} + h_\psi \frac{\partial}{\partial \psi}\overline{\varepsilon}_\psi(\psi,t)\frac{\partial \dot{\Phi}}{\partial \psi} = -4\pi e \Delta\rho, \tag{7}$$

where divergence of the integrated perpendicular current is

$$\Delta\rho(\psi,\varphi,t) \equiv \frac{\partial}{\partial \varphi}\left(c\rho\frac{\partial \Phi}{\partial \psi} + c\tilde{N}_i \left\| \frac{|\nabla\varphi|^2}{\omega_{ci}B} \right\| \frac{\partial \dot{\Phi}}{\partial \varphi} + \sum_\mu \omega_d(\mu,\psi)F_\mu \right) - \frac{\partial}{\partial \psi} \times \left(c\rho\frac{\partial \Phi}{\partial \varphi} - c\tilde{N}_i \left\| \frac{|\nabla\psi|^2}{\omega_{ci}B} \right\| \frac{\partial \dot{\Phi}}{\partial \psi} \right), \tag{8}$$

and the time-dependent, axisymmetric dielectric functions are

$$\overline{\epsilon}_\varphi(\psi,t) = 1 + 4\pi e c \frac{\overline{N_i}}{h_\varphi}\left\| \frac{|\nabla\varphi|^2}{\omega_{ci}B} \right\| \approx 0.3\frac{\langle\overline{\omega_{pi}^2}\rangle}{\omega_{ci}^2}, \tag{9}$$

$$\overline{\epsilon}_\varphi(\psi,t) = 1 + 4\pi e c \frac{\overline{N_i}}{h_\psi}\left\| \frac{|\nabla\psi|^2}{\omega_{ci}B} \right\| \approx 0.18\frac{\langle\overline{\omega_{pi}^2}\rangle}{\omega_{ci}^2}. \tag{10}$$

In CTX, $\langle\overline{\omega_{pi}^2}\rangle/\omega_{ci}^2 \sim 10^3$ and scales with radius as $\propto \overline{N_i}/\psi^2$. Equation (7) requires the most computation to solve since, at each time step, we iteratively invert the Laplacian operator on the left-hand side (LHS) to arrive at improved approximations to $\dot{\Phi}$ which also appears on the right-hand side (RHS).

B. Numerical methods

The nonlinear evolution of the hot electron interchange instability is simulated by computing solutions to Eqs. (4), (6), and (7) on uniform, rectangular grids, 64×64, in the (ψ,φ) plane. We use the fourth-order flux-corrected transport (FCT) method developed by Zalesak[40,41] and a second-order trapezoidal leap-frog algorithm for the time integration.[42] We also add a constant and uniform dissipation to the equation advancing the electrostatic potential. This term prevents numerical instability at short wavelengths and, additionally, represents a physically relevant nonresonant dissipation of potential oscillations. As predicted by Berk,[37] we find the rate of frequency chirping to be proportional to this dissipation. Finally, we set the boundaries of $\Phi(\psi,\varphi,t)$ to be zero both at $\psi=\psi_{\max}$, corresponding to the surface of the terrella, and at $\psi_{\min}$, corresponding to the surface of the vacuum vessel. The precise definition of $\psi_{\max}$ influences the global mode structure, and a good fit to the measured mode structure results for a reasonable value of $\psi_{\min}$.

To illustrate these numerical methods, note that the conservation equations determining the evolution of $N_i(t)$ and $F_\mu(t)$ have the general form $\dot{f} = -\nabla\cdot\Gamma(f(t),\Phi(t),\dot{\Phi}(t))$, with f representing either N_i or one of several F_μ and with Γ representing the field-line integrated particle flux. At the beginning of every time step, $f(t)$, $\Phi(t)$, and $\dot{\Phi}(t)$ are known throughout the computational (ψ,φ) domain and at a previous step, $t-\Delta t$. For these equations, the second-order leap-frog and trapezoidal steps are taken as

$$f^*_{t-\Delta t/2} = \tfrac{1}{2}(f_t + f_{t-\Delta t}), \tag{11}$$

$$f^*_{t+\Delta t/2} = f^*_{t-\Delta t/2} - \Delta t\Delta\Gamma(f(t),\Phi(t),\dot{\Phi}(t)), \tag{12}$$

$$f_{t+\Delta t} = f_t - \Delta t\Delta\Gamma(f^*(t+\Delta t/2),\Phi^*(t+\Delta t/2),\dot{\Phi}^*(t+\Delta t/2)). \tag{13}$$

The fourth-order, finite-difference expression for $\nabla\cdot\Gamma$ is written plainly as $\Delta\Gamma(\cdots)$, but this operator represents Zalesak's three step FCT process: compute the result of low-order convection, find the high-order, flux-limiting antidiffusive fluxes, and compute the limited fourth-order convection such that no new extrema are created nor existing extrema accentuated.

The electrostatic potential must be advanced with N_i and F_μ, and this is done while preserving second-order accuracy in time and fourth-order accuracy on the spatial grid. At each time step and at each half-step in Eq. (13), $\dot{\Phi}$ is determined by Eq. (7). The Laplacian is inverted with fast-Fourier transforms along φ, the fixed boundaries $\dot{\Phi}=0$ at $\psi_{\max}$ and $\psi_{\min}$, and the known values of N_i, F_μ, and Φ. We choose to treat the appearance of $\dot{\Phi}$ on the RHS of Eq. (7) using iteration. Successively more accurate solutions to Eq. (7) are found by inverting the LHS until the difference between $\dot{\Phi}$ on the LHS and the RHS effectively vanishes. (We find this convergence to be rapid, requiring less than ten iterations.)

With $\dot{\Phi}$ determined, Φ is also time advanced with trapezoidal leap-frog steps. In order to prevent short-wavelength numerical instability and to introduce nonresonant dissipation (which controls frequency sweeping), dissipation is added as the potential is advanced in time. Since the flux-corrected transport of the electrons and ions introduces very little numerical dissipation, this explicit dissipation, even when very small, dominates over any artificial, numerical damping. With $\dot{\Phi}(t)$ determined from $N_i(t)$, $F_\mu(t)$, and $\Phi(t)$ and $\dot{\Phi}^*(t+\Delta t/2)$ determined from $N_i^*(t+\Delta t/2)$, $F_\mu^*(t+\Delta t/2)$, and $\Phi^*(t+\Delta t/2)$, the potential is advanced according to the rule

$$\Phi^*_{t-\Delta t/2} = \tfrac{1}{2}(\Phi_t + \Phi_{t-\Delta t}), \tag{14}$$

$$\Phi^*_{t+\Delta t/2} = \Phi^*_{t-\Delta t/2} + \Delta t\dot{\Phi}_t - (-1)^k \Delta t\,\nu\nabla^{2k}\Phi_t, \tag{15}$$

$$\Phi_{t+\Delta t} = \Phi_t + \Delta t\dot{\Phi}^*_{t+\Delta t/2} - (-1)^k \Delta t\,\nu\nabla^{2k}\Phi^*_{t+\Delta t/2}. \tag{16}$$

The term proportional to the constant ν weakly damps potential oscillations. The integer $k=0,1,2,...$ sets the scale length for dissipation. Although we have examined solutions with k ranging from 0 to 4, for the results discussed here, we set $k=2$, and ν ranged from 0.003 to 0.01 times the grid-scale normalization, $\sim(1/64)^2\omega_{d0}$.

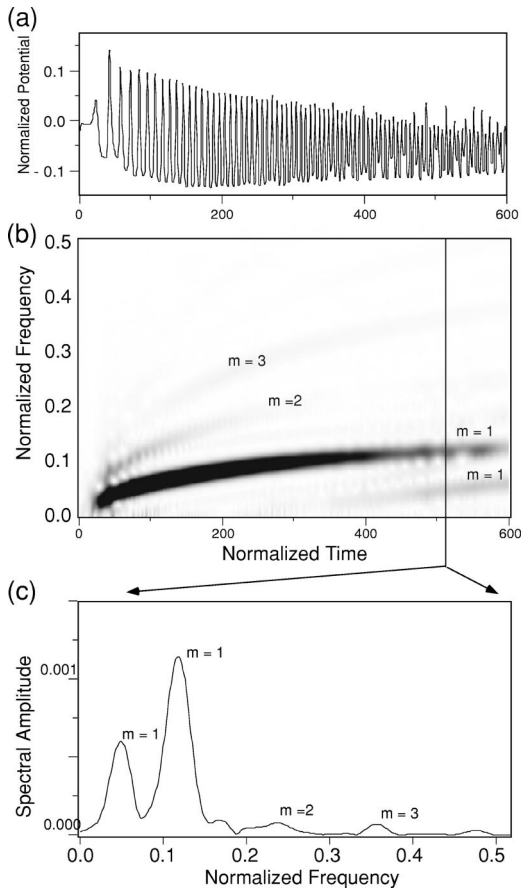

FIG. 7. Self-consistent time evolution of the electrostatic potential computed using the nonlinear simulation. The TFD of the potential oscillations computed by the simulation show multiple modes and frequencies rising in time that resembles Figs. 2 and 3. Time is normalized to ω_{dh0}^{-1}, and the potential is normalized to $\mu_0 B_0/e$.

C. Global mode structure comparison

The numerical solutions exhibit many characteristics observed in the experiment.[30] For example, the HEI instability is destabilized only for a sufficiently large fraction of energetic electrons. The simulation also shows frequency chirping, multiple azimuthal modes, and strong modulation of energetic electron flux during nonlinear saturation. Figure 7 illustrates the time evolution of the electrostatic potential as computed by the simulation from initial conditions consistent with the experiment. The instability grows quickly to large amplitude, $e|\Phi| \sim 0.1\mu_0 B_0$, and develops a relatively complex, time-evolving frequency spectrum with $\dot{\omega}/\omega^2 \approx 0.09$. Azimuthal modes with $m=1$, 2, and 3 can be detected easily, and the global structure of these modes can be ''measured'' by computing the Fourier transforms of the simulated potential. In this section, the initial conditions for this solution are described, and the computed global mode structure is compared with measurements.

The initial potential fluctuations are set to randomly phased, low-amplitude oscillations that vary sinusoidally in both the ψ and φ directions. The initial profiles of the ions and the energetic electrons are axisymmetric with an initial radial variation of the form $f(\psi, t=0) \propto (\psi_{\max} - \psi)^b (\psi - \psi_{\min})^c$, where the parameter b is chosen to insure $\partial f/\partial \psi = 0$ at $\psi = \psi_0$ and c is adjusted to change the steepness of the profile. For the energetic electrons, $c=4$ and $b=2.46$. For the ion number density, the initial profile was the sum of two equal parts: a constant and a gradual radial variation with $c=1$ and $b=0.62$. At the density peak, $R=R_0$, half of the electrons were energetic and half were cold.

The distribution of energetic electrons are modeled with five energy groups, $F(\mu, \psi, \varphi) = \alpha(\psi) \Sigma_{i=1}^{5} \beta(\mu = \mu_i)$, with $\mu_i/\mu_0 = 0.5$, 0.75, 1.0, 1.25, and 1.5. The initial radial profile, $\alpha(\psi)$ has the form described above, and the initial profile for each electron group is identical. The function $\beta(\mu) \propto (2\mu/\mu_0)\exp(-2\mu/mu_0)$ determines the relative number density of each of the five groups of energetic electrons. As the instability develops, resonant electrons are strongly mixed in radius; however, the total number of electrons with each value of magnetic moment is constant.

In Fig. 7, the normalized dissipation rate was $\nu = 0.005$. For global modes, this causes a nonresonant damping of the order, $\partial \log \Phi/\partial t \sim 10^{-5} \omega_{d0} \ll \omega$. For broad, long-wavelength modes, this is a very small dissipation rate, but it nevertheless influences the solution significantly. If ν is decreased to 0.003, the frequency changes more slowly in time, $\dot{\omega}/\omega^2 \approx 0.07$. If ν is increased to 0.01, the frequency ''chirps'' more rapidly, $\dot{\omega}/\omega^2 \approx 0.2$.

The global structures of the modes simulated numerically are viewed by performing Fourier transforms of the computed potential, $\Phi(\psi, \varphi)$. The relative radial variations of the amplitude and phase of an azimuthal mode, $\Phi_m(\psi)$, can be compared directly with experimental measurements.

When this comparison was first made, we noticed a sensitivity to the location of the outer boundary, $\psi = \psi_{\min}$, where Φ is forced to vanish. When $\psi_{\min}$ was set to correspond to the inner radius of the vacuum vessel, $R=67$ cm and $\psi_{\min}/\psi_0 = 0.4$, the computed mode structures were more peaked than seen experimentally. As the outer boundary was moved to larger radii, the global modes in the simulation broadened. Several simulations were computed as the outer boundary gradually increased to $R=98$ cm, or $\psi_{\min}/\psi_0 = 0.27$. From these we were able to identify the outer location that minimized the magnitude of the difference between the simulated and measured mode structures for the lowest three modes, $m=1$, 2, and 3. This occurred when $R_{\max}=77$ cm, or $\psi_{\min}/\psi_0 = 0.35$. If only one mode (instead of three) was compared, the optimal location for the outer boundary was different. The $m=1$ mode optimized at larger $R_{\max}$ while $m=3$ optimized at slightly smaller $R_{\max}$.

While we are not certain of the reason why a larger diameter of the outer boundary is required for the simulation to match the experiment's mode structures, we believe it results from the large geometric difference between the cylindrical vacuum vessel and the dipole's field lines. As shown in Fig. 1, the field lines are tangent to the vacuum vessel at $R=67$ cm. This limits the extent of energetic electrons, but not the colder plasma. As a Langmuir probe is moved out ward, beyond the last flux tube not obstructed by the vessel, the plasma density drops abruptly by more than a factor of 2, but this does not eliminate HEI potential fluctuations. Obviously, the experimental boundaries are much more complex

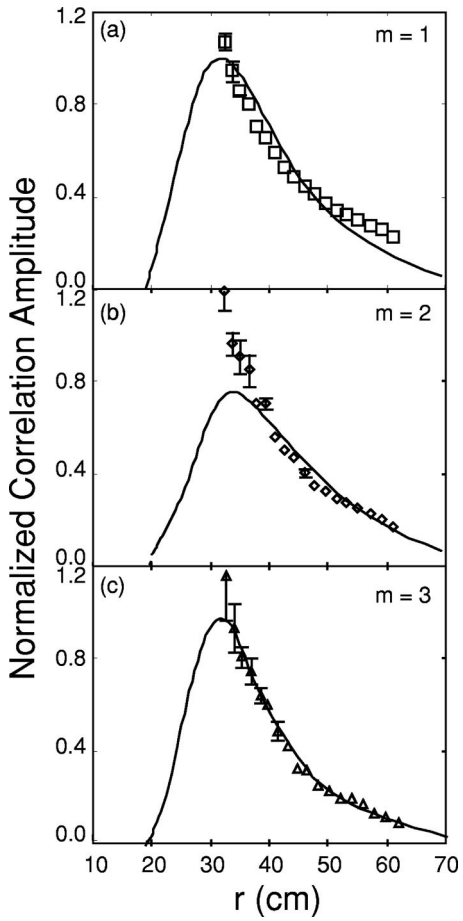

FIG. 8. Comparison of radial mode structure computed from the nonlinear simulation (solid lines) with the observed profiles of the normalized correlation amplitudes for $m=1$, 2, and 3.

than simulated, and it is perhaps not surprising that some adjustment is required to match these conditions.

The computed nonlinear global mode structures are shown in Figs. 5 and 8 when the outer boundary was set to $R_{\max}=77$ cm. Radial profiles of the radial phase difference, $k_R\Delta R$, generated from the simulation for $m=1$, 2, and 3 are shown as solid lines in Fig. 5 (and superimposed onto the experimental data). The computed phase difference with radius is small. As in the experiment, the modes rotate rigidly with $k_R\sim 0$. Figure 8 compares the radial variation of the mode amplitudes with the observed normalized correlation amplitudes (which are also shown in Fig. 6). As seen experimentally, the ratios of the mode amplitudes evolve in time, but the form of radial structures are essentially constant once the amplitude saturates. In Fig. 8, the computed mode amplitudes were normalized to minimize the least square difference between simulation and experiment. The profiles are peaked near the peak of the energetic electron density at $R_0=27$ cm. Modes with higher m are more centrally peaked than modes with lower m.

The model equations give insight into the electrostatic potential structures of different azimuthal modes. If the net oscillating charge on the flux tubes, ρ, were nonzero only near the peak density of the energetic electrons (e.g., $R\approx 27$ cm), then Eq. (7) can be used to solve for the radial mode structure by separation of variables. Let $\Delta\rho\rightarrow 0$ except for a narrow region near $\psi\approx\psi_0$, and let the potential have the form $\Phi(\psi,\varphi,t)=g(\psi)\exp[-i(\omega t-m\varphi)]$. If we further take N_i to be a constant in order to simplify the form of the plasma dielectric [Eqs. (9) and (10)], then the radial structure function, $g(\psi)$, must satisfy the equation

$$\psi^4\frac{\partial}{\partial\psi}\left(\frac{1}{\psi^2}\frac{\partial g_m}{\partial\psi}\right)-0.83m^2g_m=0. \tag{17}$$

With the vacuum vessel wall at infinity, the outer solutions have a simple form $g_m\sim\psi^a\sim 1/R^a$ where $a=3/2+\sqrt{9/4+0.833m^2}$. The lowest three azimuthal modes are $g_1\sim 1/R^{3.3}$, $g_2\sim 1/R^{3.9}$, and $g_3\sim 1/R^{4.6}$. These expressions are reasonably close to the radial dependencies shown in Figs. 6 and 8, although the actual mode structures are less peaked. Equation (17) also offers a simple and perhaps general explanation of our key results. Indeed, during the simulation, $\rho(\psi,\varphi,t)$ is monitored, and, the largest oscillations or ρ do not occur near the peak of the energetic electrons.

The inner structures of the global modes could not be measured. As probes moved inward, the intensity of the artificial radiation belt was significantly perturbed. For this reason, we are unable to make any conclusions pertaining to the inner boundary condition at the surface of the dipole magnetic nor the mode structures near and within the radius of peak energetic electron density.

V. SUMMARY

The global mode structure of low frequency interchange instabilities driven by energetic electrons was measured using time-frequency-domain analysis of the correlations between multiple high-impedance probes. A modal prescription was used to simplify the correlation analysis of movable high impedance floating potential probes. By positioning the probes appropriately, the HEI instability was seen to be flute-like with $k_\parallel\sim 0$ with multiple azimuthal modes peaked in amplitude near the peak density of energetic electrons. The modes have a time-evolving frequency spectrum, but the form of the global mode structure does not change significantly in time. The radial mode structures are relatively broad, and they rotate rigidly with $k_R\Delta R\approx 0$.

A nonlinear, self-consistent numerical simulation of the growth and saturation of the HEI instability reproduces many observations from the experiment including the radial structures of the lowest azimuthal modes. The agreement between the modes computed by the simulation and the experimental measurements supports the underlying assumptions of the model equations and the resonant phase-space dynamics reported previously.[30]

Although general characteristics of the numerical solutions to the model equation resemble experimental measurements, several observations of the HEI instability in the experiment are not modeled nor do we fully understand how to do so. During microwave heating, the quasiperiodic bursts of instability have a more complex frequency spectrum than seen computationally. Experimentally, a period of rising coherent modes occurs after a short period when the frequency spectrum is relatively broad-band and turbulent. Broad-band

fluctuations have not been seen computationally. Perhaps, most significantly, the mode structure of the HEI is sensitive to the experimental boundary conditions, and observations of the fluctuations near and within the region of energetic electrons has been so far impossible.

New experiments are underway that may provide additional insight into the structure, causes, and evolution of electrostatic interchange modes in dipole-confined plasma. In the CTX device, an array of 96 energetic particle detectors will be able to measure and to image the rapid electron dynamics during interchange mixing. In addition, thermionic filaments will be installed at the inner equator in order to inject electrons onto inner field lines. This will allow controlled charging of field lines and generate radial electric fields and strong azimuthal plasma rotation. In these future experiments, it is hoped to determine the similarities and differences between interchange motion driven by centrifugal drifts and by the magnetic drifts of energetic electrons.

ACKNOWLEDGMENTS

We gratefully acknowledge the support of AFSOR Grants F49620-97-1-0425 and F49620-97-1-0026 and US DOE Grant No. DE-FG02-00ER54585.

[1]C. L. Longmire and M. N. Rosenbluth, Ann. Phys. (N.Y.) **1**, 120 (1957).
[2]I. B. Bernstein, E. A. Frieman, M. D. Kruskal, and R. M. Kulsrud, Proc. R. Soc. London, Ser. A **244**, 17 (1958).
[3]S. Chandrasekar, *Plasma Physics* (University of Chicago Press, Chicago, IL, 1960), pp. 80–96.
[4]V. D. Shafranov, Nucl. Fusion **28**, 253 (1968).
[5]Yu V. Gott, M. S. Ioffe, and V. G. Tel'kovskii, Nucl. Fusion Suppl. **1962**, 1045 (1962); see also M. S. Ioffe, ''Mirror traps,'' *Plasma Physics* (IAEA, Vienna, 1965), pp. 421–448.
[6]C. W. Hartman, Phys. Fluids **9**, 821 (1966).
[7]R. Freeman, M. Okabayashi, G. Pacher *et al.*, ''Confinement of plasmas in the spherator,'' *Plasma Physics and Controlled Nuclear Fusion* (IAEA, Vienna, 1971), Vol. 1, pp. 27–57.
[8]J. R. Ferron, A. Y. Wong, G. Dimonte, and B. J. Leikind, Phys. Fluids **26**, 2227 (1983).
[9]D. E. Lencioni, J. W. Poukey, J. A. Schmidt, J. C. Sprott, and C. W. Erickson, Phys. Fluids **11**, 1115 (1968).
[10]M. C. Kelly, *The Earth's Ionosphere* (Academic, San Diego, CA, 1989), pp. 113–185.
[11]T. Gold, J. Geophys. Res. **64**, 1219 (1959).
[12]D. J. Southwood and M. G. Kivelson, J. Geophys. Res. **92**, 109 (1987).
[13]D. J. Southwood and M. G. Kivelson, J. Geophys. Res. **94**, 299 (1989).
[14]C.-G. Fälthammar, J. Geophys. Res. **70**, 2503 (1965).
[15]G. L. Siscoe, A. Eviatar, R. M. Thorne, and J. D. Richardson, J. Geophys. Res. **86**, 8480 (1981).
[16]R. M. Thorne, T. P. Armstrong, S. Stone *et al.*, Geophys. Res. Lett. **24**, 2131 (1997).
[17]M. G. Kivelson, K. K. Khurana, C. T. Russell, and R. J. Walker, Geophys. Res. Lett. **24**, 389 (1997).
[18]L. A. Frank and W. R. Paterson, J. Geophys. Res. **106**, 6131 (2001).
[19]S. T. Zalesak and S. L. Ossakow, J. Geophys. Res. **85**, 2131 (1980).
[20]G. A. Navratil, R. S. Post, and A. Butcher Ehrhardt, Phys. Fluids **20**, 156 (1977).
[21]F. J. Øynes, H. L. Pécseli, and K. Rypdal, Phys. Rev. Lett. **75**, 81 (1995).
[22]C. Riccardi and A. Fredriksen, Phys. Plasmas **8**, 199 (2001).
[23]K. Rypdal, O. E. Garcia, and J.-V. Paulsen, Phys. Rev. Lett. **79**, 1857 (1997).
[24]N. A. Krall, Phys. Fluids **9**, 820 (1966).
[25]H. L. Berk, Phys. Fluids **19**, 1255 (1976).
[26]W. A. Ard, R. A. Dandl, and R. F. Stetson, Phys. Fluids **9**, 820 (1966).
[27]S. Hiroe, J. B. Wilgen, F. W. Baity *et al.*, Phys. Fluids **27**, 1019 (1984).
[28]A. J. Lichtenberg and H. Meuth, Phys. Fluids **29**, 3511 (1986).
[29]D. A. Spong, H. L. Berk, and J. W. Van Dam, Phys. Fluids **27**, 2292 (1984).
[30]M. E. Mauel, J. Phys. IV **7**, 307 (1997).
[31]H. P. Warren and M. E. Mauel, Phys. Rev. Lett. **74**, 1351 (1995).
[32]H. P. Warren and M. E. Mauel, Phys. Plasmas **2**, 4185 (1995).
[33]H. P. Warren, M. E. Mauel, D. Brennan, and S. Taromina, Phys. Plasmas **3**, 2143 (1996).
[34]H. P. Warren, A. Bhattacharjess, and M. E. Mauel, Geophys. Res. Lett. **19**, 941 (1992).
[35]A. A. Chan, L. Chen, and R. B. White, Geophys. Res. Lett. **16**, 1133 (1989).
[36]H. L. Berk, B. N. Breizman, and N. V. Petviashvili, Phys. Lett. A **234**, 213 (1997).
[37]H. L. Berk, B. N. Breizman, J. Candy, M. Pekker, and N. V. Petviashvili, Phys. Plasmas **6**, 3102 (1999).
[38]D. Maslovsky, M. Mauel, and B. Levitt, ''Numerical simulation of phase-space flows in the collisionless Terrella experiment,'' IEEE Trans. Plasma Sci. (in press).
[39]C. E. McIlwain, Space Sci. Rev. **5**, 585 (1966).
[40]S. T. Zalesak, J. Comput. Phys. **31**, 335 (1979).
[41]S. T. Zalesak, J. Comput. Phys. **40**, 497 (1981).
[42]P. N. Guzdar, J. F. Drake, D. McCarthy *et al.*, Phys. Fluids B **5**, 3712 (1993).